# Wavelet Transforms for Detecting Microcalcifications in Mammograms

Robin N. Strickland,* *Senior Member, IEEE*, and Hee Il Hahn

*Abstract*— Clusters of fine, granular microcalcifications in mammograms may be an early sign of disease. Individual grains are difficult to detect and segment due to size and shape variability and because the background mammogram texture is typically inhomogeneous. We develop a two-stage method based on wavelet transforms for detecting and segmenting calcifications. The first stage is based on an undecimated wavelet transform, which is simply the conventional filter bank implementation without downsampling, so that the low-low (LL), low-high (LH), high-low (HL), and high-high (HH) sub-bands remain at full size. Detection takes place in HH and the combination LH+HL. Four octaves are computed with two inter-octave voices for finer scale resolution. By appropriate selection of the wavelet basis the detection of microcalcifications in the relevant size range can be nearly optimized. In fact, the filters which transform the input image into HH and LH+HL are closely related to prewhitening matched filters for detecting Gaussian objects (idealized microcalcifications) in two common forms of Markov (background) noise. The second stage is designed to overcome the limitations of the simplistic Gaussian assumption and provides an accurate segmentation of calcification boundaries. Detected pixel sites in HH and LH+HL are dilated then weighted before computing the inverse wavelet transform. Individual microcalcifications are greatly enhanced in the output image, to the point where straightforward thresholding can be applied to segment them. FROC curves are computed from tests using a freely distributed database of digitized mammograms.

## I. INTRODUCTION

THE early detection of small, nonpalpable breast cancers is the aim of screening mammography. An early sign of disease in 30–50% of mammographically detected cases is the appearance of clusters of fine, granular microcalcifications ($\mu$Ca++s) whose individual grains typically range in size from 0.05–1 mm in diameter [1]–[6]. Individual $\mu$Ca++s are difficult to detect because of variations in their shape and size and because they are embedded in and camouflaged by varying densities of parenchymal tissue structures. Indeed, recent estimates indicate that between 10 and 30% of breast lesions (of all types) are missed by radiologists during routine screening [7]–[11]. Computer-aided diagnosis (CAD) schemes using digital image processing techniques have the goal of improving the detection performance and throughput

of screening mammography. Typically, CAD systems are designed to provide a "second opinion," to aid rather than replace the radiologist. The literature documents a number of approaches to $\mu$Ca++ detection [12]–[23].

An important branch of CAD methods in mammography employs wavelet transforms for feature enhancement [24]–[29]. The general approach is 1) Compute the forward wavelet transform of the image, 2) nonlinearly transform or adaptively weight the wavelet coefficients, and 3) compute the inverse wavelet transform. Richardson [24] showed that the details components of the lowest octaves (i.e., those containing the finest structure) can be useful in enhancing the visibility of $\mu$Ca++s. Laine [25] achieves a scale-dependent enhancement of mammograms by selectively weighting and scaling the details computed using a first derivative of a Gaussian wavelet. In later work [26] a dyadic wavelet transform method is shown to be equivalent to unsharp masking at multiple scales. Barman [27] employs a hybrid of wavelet and feature extraction techniques for $\mu$Ca++ detection. The outputs from multiple scale quadrature filters are processed by specialized object extraction algorithms employing size, orientation, relative brightness and shape features. Clusters of $\mu$Ca++s are tagged by examining and detecting likely combinations of features in the object list. Qian *et al.* [28] enhance $\mu$Ca++s by cascading adaptive spatial filtering with multiresolution decomposition and reconstruction. Yoshida *et al.* [29] improve the visibility of $\mu$Ca++s by reconstructing mammograms from selected subbands. Post-detection using morphological operators and thresholding achieves a sensitivity of 85% true clusters detected at five false positive clusters per image when tested on a 100-$\mu$m resolution database of 39 mammograms. The authors conclude that wavelet techniques are especially useful for detecting subtle $\mu$Ca++s when used to augment existing CAD algorithms.

Our contribution to the application of wavelets in mammography is to employ a wavelet transform which acts as a bank of multiscale matched filters for detecting $\mu$Ca++s. The sub-band images created by a four-octave wavelet decomposition are thresholded and combined to yield a map of detected pixels. Segmentation of $\mu$Ca++s is realized by weighting the sub-bands at these detected sites before computing the inverse wavelet transform. Depending on which sub-bands of the forward wavelet transform are included in the inverse operation, the reconstructed image may consist of detected pixels only, or detected pixels superimposed on the original mammogram. The basic wavelet transform is implemented at full resolution in each octave level, with additional "voices" inserted between octaves to provide improved scale resolution.

After giving details of the method, we present a performance curve resulting from tests on a set of 40 digital mammograms and show examples of reconstructed calcifications.

## II. DATA

### A. Mammogram Database

We test our $\mu$Ca++ detection algorithms on a database of 40 mammograms created by N. Karssemeijer of University Hospital Nijmegen, The Netherlands [19], [20]. The mammograms were recorded with a Kodak MIN-R/SO177 screen/film combination. Each image was digitized from film using an Eikonix 1412 CCD camera operating at a spatial resolution of 2048 × 2048 pixels per image with 12 bits per pixel, with a sampling aperture of 50 $\mu$m in diameter and a 100-$\mu$m sample spacing. The 40 images represent 21 different patients. Each image contains one or more calcification clusters verified by expert radiologists and histology. The database contains a total of 104 clusters, many of which proved to be malignant. One pair of images, numbered 12o (oblique) and 12c (craniocaudal), contains a total of 28 clusters, which is approximately 27% of the total. The remaining images each contain an average of two clusters. Ground truth for each image consists of the $x, y$ coordinates and the diameter of a "truth circle" for each verified cluster. The locations of individual $\mu$Ca++s are not marked. The visibility of the clusters is highly variable, which is rather typical of clinical cases. In a preprocessing step, each image is gray-scale transformed using a noise-equalizing look-up table. (Look-up tables are distributed with the database. See [20] for details.)

### B. Cluster Detection Criteria

At present no universally accepted criteria for the detection of clustered $\mu$Ca++s have been agreed upon, although various research groups are currently attempting to assemble a common database of mammograms with ground truth and a set of standardized detection metrics. We adopt the detection criteria proposed by Karssemeijer [19]; namely that for counting true positives (TP's) a cluster is considered detected if two or more $\mu$Ca++s are found in the region of film (truth circle) identified by the radiologist. A false positive (FP) is counted if two or more erroneous detections are made within an empty, closed region of 0.5 cm in width. One weakness of this metric is that at high sensitivity thresholds the number of false positives may actually drop due to merging of previously separated false clusters. In practice, however, this occurs at false positive rates which are too high to be of any clinical value. The useful part of the performance curve lies below one or two false clusters per image.

### C. Characteristics of Microcalcifications

Individual $\mu$Ca++s appear as small (typically 0.05–1 mm) particulate objects of variable shape (from granular to rod-shaped) and fairly uniform optical density. Although $\mu$Ca++s vary in outline and degree of elongation, the *average* form is roughly circular, with a tapered cross-sectional profile. Fig. 1(a) shows the cross section of a typical cluster with
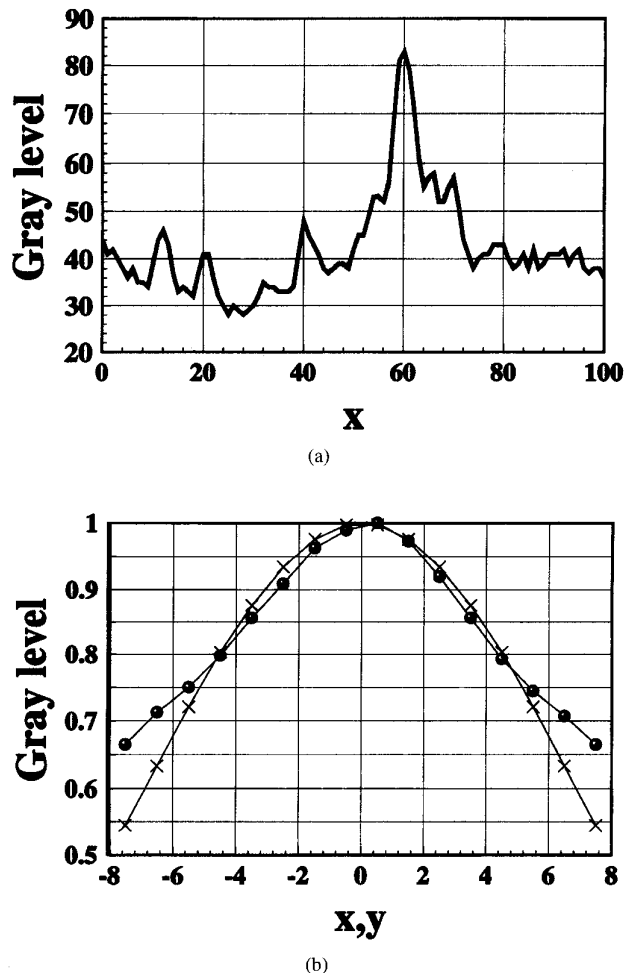


Fig. 1. (a) Cross section of a prominent $\mu$Ca++ cluster. (b) Average of $x$ and $y$ profiles (o) of a random sample of 80 $\mu$Ca++s, after normalizing for variations in height and width. A Gaussian curve (×) fit is shown.

four prominent $\mu$Ca++s. Fig. 1(b) shows the average profile computed from 80 $\mu$Ca++s selected at random from the test images. For a given size, it is not unreasonable to model the *average* $\mu$Ca++ using a circularly-symmetric Gaussian function. [See Fig. 1(b)]. Another merit of the Gaussian model is that it leads to separable detection filters which are implementable via the wavelet transform. Furthermore, the wavelet transform causes smoothing and even better agreement to the Gaussian. In our work we adopt the Gaussian model for $\mu$Ca++ *detection*. A separate *segmentation* step does not rely on the Gaussian assumption.

### D. Model of Mammogram Texture

The visibility of $\mu$Ca++s is often degraded by the high frequency texture of breast tissue. For designing detectors, a statistical model of this background noise texture is required. A widely used stochastic model of images [32] consists of a nonstationary mean plus a stationary "residual" component modeled as either a *separable* Markov process with autocorrelation $r_{nn}(k, l) = \sigma_n^2 e^{-\alpha(|k|+|l|)}$, or a *nonseparable* Markov
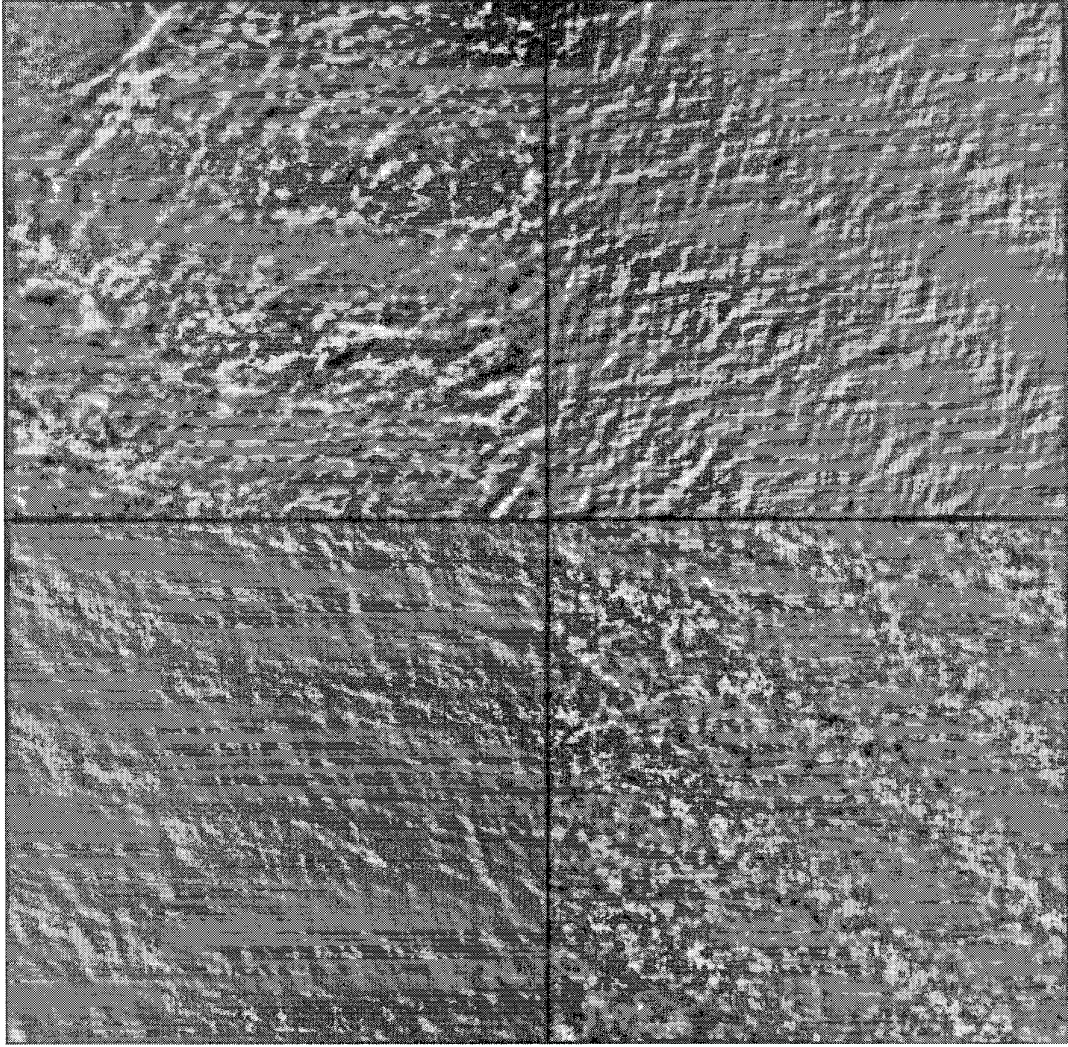
Fig. 2. Markov model of high frequency mammogram texture. (upper left) Sample mammogram with spatial mean removed, which we call the "residual" component, (upper right) separable Markov model texture with $\alpha = 0.2$, (lower left) nonseparable Markov texture with $\alpha = 0.01$, and (lower right) weighted average of the two texture types. This synthetic texture closely matches the residual mammogram.

process with autocorrelation $r_{nn}(k,l) = \sigma_n^2 e^{-\alpha\sqrt{k^2+l^2}}$ [33]. The residual component is typically created by subtracting a low-pass filtered version of the image from the original image. The residual image, since it contains the high frequency details of the image, is a logical choice for representing mammogram texture. Fig. 2 compares simulated textures with the residual texture computed from a sample mammogram. The nonseparable Markov texture is isotropic, which would appear to be better suited for breast texture, with its structures oriented in all directions. Nevertheless, the horizontal and vertical streaking generated by the separable model may be useful for representing the fine vasculature of the breast. In fact, as this figure suggests, a combination of separable and nonseparable models may be closest to the truth.

After subtracting the spatial mean from each mammogram, the Markov correlation parameter $\alpha$ of the residual process is estimated using [34] $\hat{\alpha} = -\ln(\hat{r}_{nn}(0,1)/\hat{r}_{nn}(0,0))$, where $\hat{r}_{nn}(k,l)$ is the estimated autocorrelation of background tex-

ture. Values of $\hat{\alpha}$ computed from images in the Nijmegen database fall in the range $0.01 \rightarrow 0.2$.

### III. MATCHED FILTER FOR DETECTING MICROCALCIFICATIONS

Consider the scenario wherein a deterministic object $f(x,y)$ (i.e., an idealized $\mu$Ca++) located at $(x_o, y_o)$ is imaged in the presence of some background noise field $n(x,y)$ (high frequency texture of breast tissue). Suppose for the moment that the noise is stationary with power spectrum $S_{nn}(\omega_x, \omega_y)$. Then the optimum detector for finding the known $f(x,y)$ is the prewhitening matched filter [30] with transfer function

$$H_{\mathrm{MF}}(\omega_x, \omega_y) = \frac{F^*(\omega_x, \omega_y)}{S_{nn}(\omega_x, \omega_y)} \exp[-j(\omega_x x_o, \omega_y y_o)]. \quad (1)$$

Detection is accomplished by sampling the filter's output at the point of peak correlation; the signal is deemed present if the output exceeds a chosen threshold. In imaging applications, the location of an object to be detected is unknown, in which case

any above-threshold correlation peaks are counted as positive detections.

The matched filter can never be optimum for detecting $\mu$Ca++s in mammograms since 1) $\mu$Ca++s vary in size and shape, thus $f(x,y)$ is not known precisely, and 2) the background texture $n(x,y)$ is nonstationary, meaning that $S_{nn}(\omega_x, \omega_y)$ is indeterminate and hence true prewhitening is unrealizable. Nevertheless a practical algorithm can be implemented with an acceptable drop in performance [31]. As discussed above, the profile of many $\mu$Ca++s is approximately Gaussian, and may be modeled as such. As for the background noise, we may adopt the Markov process model with power spectrum $S_{nn}(\omega_x, \omega_y)$. Under these assumptions it is feasible to derive the matched filter in (1) for application to the residual component, i.e., after subtracting the spatial mean from the image.

Hence if we assume that the signal to be detected is the Gaussian $f(x,y) = e^{-((x^2+y^2)/2\sigma^2)}$, then the *separable* prewhitening matched filter is

$$H_{\text{sep}}(\omega_x, \omega_y) = H_{mf}(\omega_x)H_{mf}(\omega_y) \qquad (2)$$

where, for $\alpha \ll 1$

$$H_{mf}(\omega) \simeq \frac{\sigma\sqrt{\pi}\omega^2}{\sqrt{2}\alpha\sigma_n}e^{-(\sigma^2\omega^2/2)}. \qquad (3)$$

Likewise, the *nonseparable* prewhitening matched filter is

$$H_{\text{nonsep}}(\omega_x, \omega_y) \approx \frac{\pi\alpha^2\sigma^2}{\sigma_n^2}\left(1+\frac{\omega_x^2}{\alpha^2}+\frac{\omega_y^2}{\alpha^2}\right)e^{-(\sigma^2(\omega_x^2+\omega_y^2)/2)} \qquad (4)$$

or, for $\alpha \ll 1$

$$H_{\text{nonsep}}(\omega_x, \omega_y) \simeq \frac{\pi\sigma^2}{\sigma_n^2}(\omega_x^2 + \omega_y^2)e^{-(\sigma^2(\omega_x^2+\omega_y^2)/2)}. \qquad (5)$$

When $\alpha \to \infty$ the residual component is already white, and the point spread functions $h_{\text{sep}}(x,y)$ and $h_{\text{nonsep}}(x,y)$ are Gaussian. (Note, however, that this condition is not apparent here due to the restriction that $\alpha \ll 1$.) When $\alpha \ll 1$ the increasing interpixel correlation of the residual causes both point spread functions to develop increasingly negative side lobes on either side of the positive main lobe, as shown in Fig. 3.

The remaining variable—the size of the $\mu$Ca++—may be accommodated by implementing a bank of both forms of matched filter in the form of a wavelet transform. The choice of an appropriate wavelet and how it can implement multiscale matched filters is discussed next.

## IV. WAVELET TRANSFORM

The reader is assumed to be familiar with the principles of one-dimensional (1-D) and two-dimensional (2-D) sub-band decomposition and the wavelet transform. For a tutorial see [35]. Here, we introduce the notation of a biorthogonal wavelet basis which is then used for $\mu$Ca++ detection.
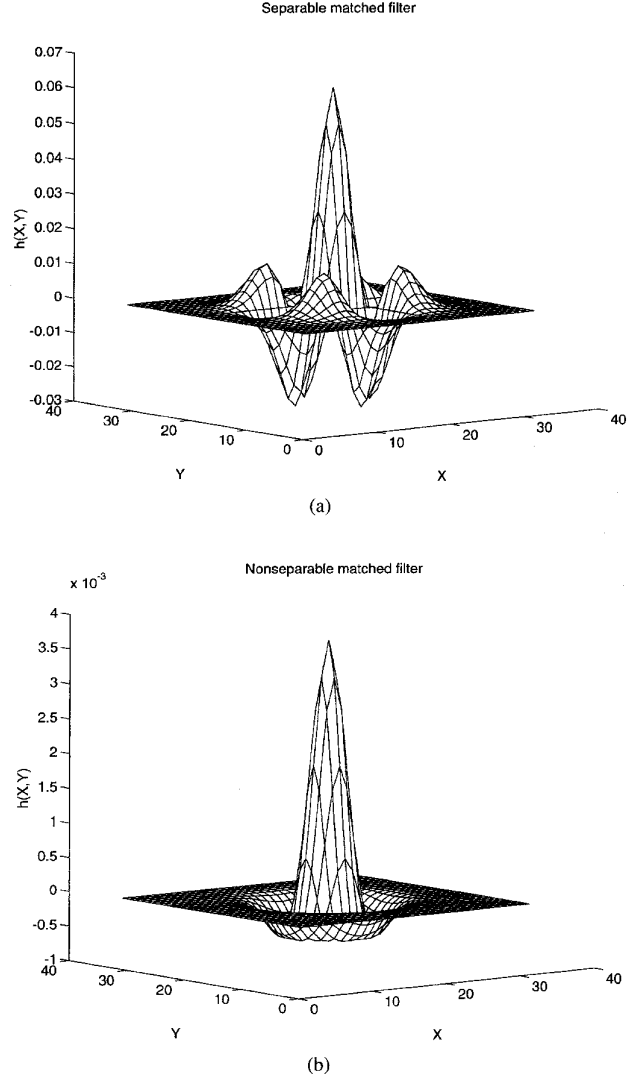


Fig. 3. Point spread functions of (a) separable and (b) nonseparable matched filters for detecting Gaussian objects in Markov noise.

### A. Biorthogonal Wavelet Bases

The biorthogonal wavelet transform uses two different wavelet bases: $\psi(x)$ for decomposition (analysis) and $\tilde{\psi}(x)$ for reconstruction (synthesis). As seen in Fig. 4, the forward 2-D wavelet transform is implemented using a bank of 1-D lowpass $(h(x))$ and highpass $(g(x))$ analysis filters. The reconstruction process, or inverse wavelet transform, is likewise computed via 1-D synthesis filters, $\tilde{h}(x)$ and $\tilde{g}(x)$. These filters must satisfy

$$H(\omega)\tilde{H}(\omega) + G(\omega)\tilde{G}(\omega) = 1$$

$$g(x) = (-1)^{x-1}\tilde{h}(1-x)$$
$$\tilde{g}(x) = (-1)^{x-1}h(-1-x). \qquad (6)$$

Furthermore, the analysis filters can be expressed as

$$H(\omega) = \frac{\tilde{\Phi}(2\omega)}{\tilde{\Phi}(\omega)} \qquad G(\omega) = \frac{\tilde{\Psi}(2\omega)}{\tilde{\Phi}(\omega)} \qquad (7)$$
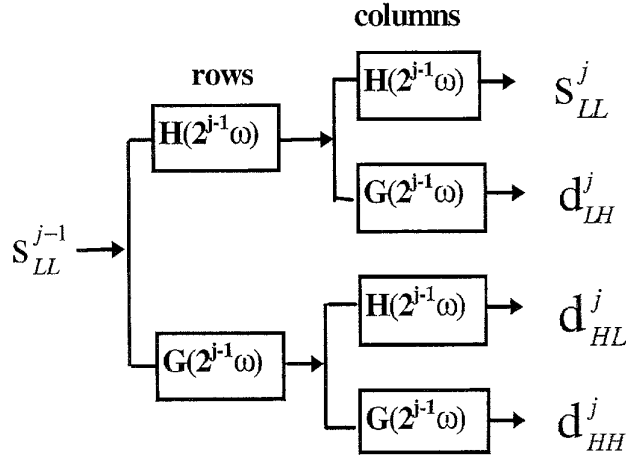
Fig. 4. Filter bank implementation of the undecimated wavelet transform. One octave level of the sub-band decomposition is shown.

TABLE I
FILTER COEFFICIENTS FOR THE ANALYSIS $(h)$ AND
SYNTHESIS $(\tilde{h})$ BIORTHOGONAL B-SPLINE WAVELET BASIS

| $n$ | $h$ | $\tilde{h}$ |
|---|---|---|
| 0 | 0.602949 | 0.557543 |
| $\pm 1$ | 0.266864 | 0.295636 |
| $\pm 2$ | $-0.078223$ | $-0.028772$ |
| $\pm 3$ | $-0.016864$ | $-0.045636$ |
| $\pm 4$ | 0.026749 | 0 |

where $\tilde{\Psi}(\omega)$ and $\tilde{\Phi}(\omega)$ are the Fourier Transforms of the synthesis *wavelet* $\tilde{\psi}(x)$ and *scaling function* $\tilde{\phi}(x)$, respectively.

The wavelet bases selected for object detection are the biorthogonal B-spline functions proposed by Cohen *et al.* [36]. Filter coefficients for $h(x)$ and $\tilde{h}(x)$ are listed in Table I. The spline basis belongs to the second-derivative or Laplacian of Gaussian class.

The three "details" images $\{d^j_{\mathrm{LH}}, d^j_{\mathrm{HL}}, d^j_{\mathrm{HH}}\}$—or simply termed low-high (LH), high-low (HL), and high-high (HH)—correspond to specific, nonoverlapping frequency bands. The LH sub-band is formed by low-pass filtering the rows followed by high-pass filtering the columns, and is therefore sensitive to horizontally oriented features. In the same way the HL sub-band contains vertically oriented structure, and the HH sub-band contains primarily diagonal structure. The low-low (LL) component is a low-pass filtered or "smooth" version of the original image, and is passed through to the next octave for further sub-band decomposition. Thus, the LL band of the frequency domain is segmented into four sub-bands at the second octave level, and so on. Fig. 5 shows one octave of a sub-band decomposition computed from a section of a mammogram. The 2-D wavelet transform is inverted by filtering and combining the details images from all octaves plus the LL component from the lowest-frequency octave.

### B. Implementation in Mammography

Down-sampling and up-sampling are normally employed in the forward and inverse wavelet transforms, respectively. In our work, however, we maintain full resolution throughout the sub-band decomposition, for two reasons. First, from the point of view of a human observer it helps to display the sub-bands at full size during algorithm development simply because features are easier to see at full resolution. Second, it is easier to combine the detected pixels from each sub-band when they are at the same resolution. Although the resulting transform is highly redundant from an information theoretic point of view, it is still simple to compute and the same analysis and

synthesis filters are employed. Furthermore, unlike the wavelet transform, the undecimated wavelet transform is translation invariant [37]. The implementation of an undecimated wavelet transform in two-dimensions is shown in Fig. 4.

A second modification overcomes the limited dyadic sampling grid of the basic wavelet transform. By passing a Gaussian object of size $\sigma$ through a sub-band decomposition and recording the peak response in each octave we obtain the scale "bandwidth" of the first four octaves, and observe significant dips in coverage between octaves 2 and 3, and between octaves 3 and 4. As proposed by Rioul [38] we can remedy this by computing a separate, three octave wavelet transform using $\times\sqrt{2}$ interpolated versions of $h(x)$ and $g(x)$. Thus, octaves 2 and 3 of the modified transform fill the gaps in coverage as desired. These inserted sub-bands are known as "voices" of the original octave decomposition. The scales covered by octaves 1 through 4 (including the voices at octaves "2.5" and "3.5") occupy the range $0.5 \leq \sigma \leq 5$ which, given that a Gaussian object is visible over $\pm\sigma$ pixels, corresponds to objects of diameter $1 \rightarrow 10$ pixels, or $100 \ \mu\mathrm{m} \rightarrow 1$ mm. This, as stated earlier, is the relevant scale range for $\mu$Ca++s in the Nijmegen database.

### C. Wavelet Transform Implementation of a Bank of Multiscale Matched Filters

Next we show how the separable and nonseparable matched filters developed in (2) and (5) can be implemented via wavelet transforms using Laplacian of Gaussian wavelets. Consider the 2-D wavelet transform with input $i(x,y) = s^0_{\mathrm{LL}}(x,y)$, and sub-band components $\{s^j_{\mathrm{LL}}(x,y), d^j_{\mathrm{LH}}(x,y), d^j_{\mathrm{HL}}(x,y), d^j_{\mathrm{HH}}(x,y)\}$ in octave $j$. From (7) we obtain the four corresponding, separable transfer functions

$$P^j_{\mathrm{LL}}(\omega_x, \omega_y) = H^j_\Phi(\omega_x)H^j_\Phi(\omega_y)$$
$$P^j_{\mathrm{LH}}(\omega_x, \omega_y) = H^j_\Phi(\omega_x)G^j_\Psi(\omega_y)$$
$$P^j_{\mathrm{HL}}(\omega_x, \omega_y) = G^j_\Psi(\omega_x)H^j_\Phi(\omega_y)$$
$$P^j_{\mathrm{HH}}(\omega_x, \omega_y) = G^j_\Psi(\omega_x)G^j_\Psi(\omega_y) \tag{8}$$

where, for example, $P^j_{\mathrm{LH}}(\omega_x, \omega_y) = D^j_{\mathrm{LH}}(\omega_x, \omega_y)/I(\omega_x, \omega_y)$ etc., and

$$H^j_\Phi(\omega) = \left[\frac{\tilde{\Phi}(2^j\omega)}{\tilde{\Phi}(\omega)}\right] \qquad G^j_\Psi(\omega) = \left[\frac{\tilde{\Psi}(2^j\omega)}{\tilde{\Phi}(\omega)}\right]. \tag{9}$$
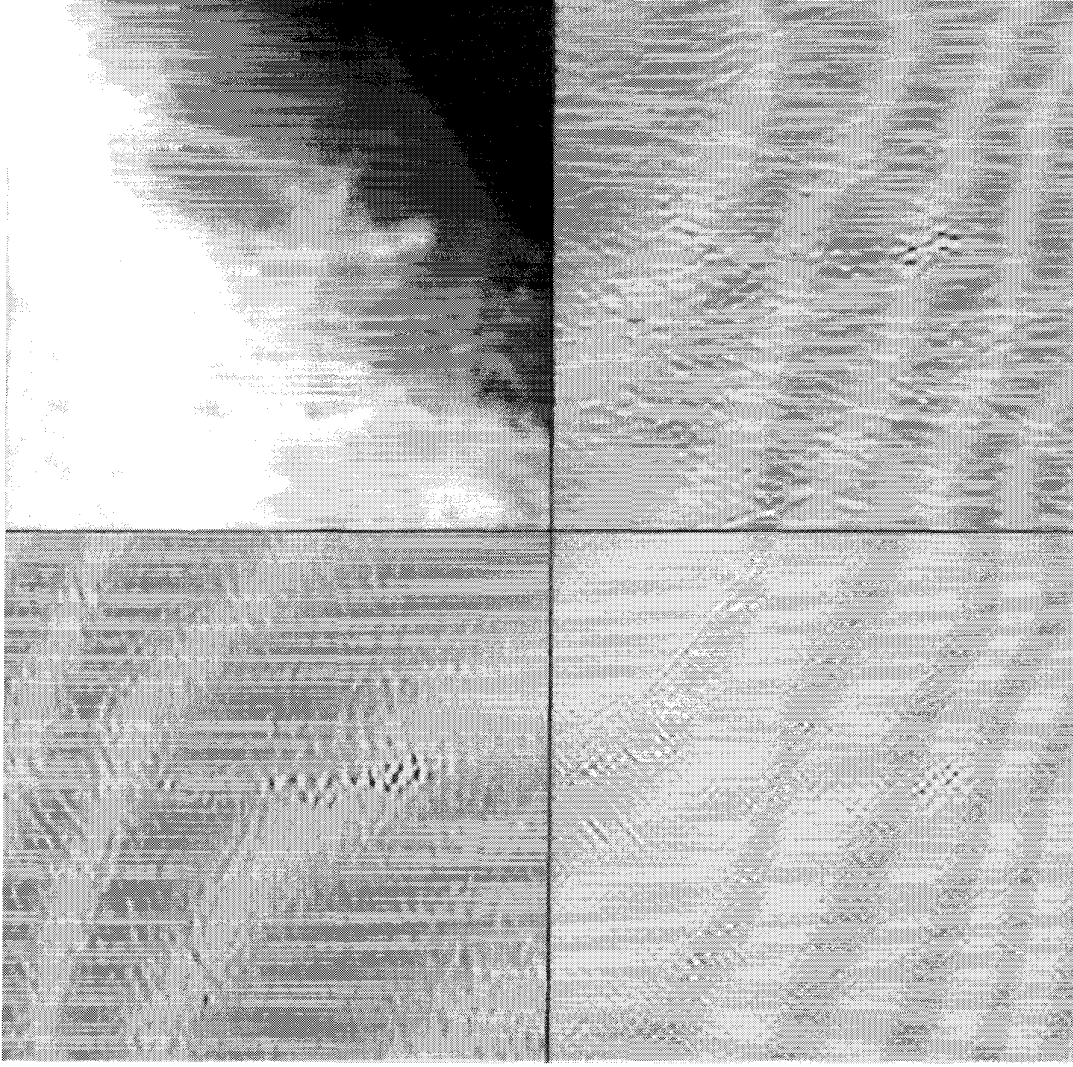
Fig. 5. (upper left) Sub-bands LL, (upper right) LH, (lower left) HL, and (lower right) HH, computed from a 512 × 512 pixel mammogram section. This is the third octave level. The wavelet basis in [36] was employed. A cluster of microcalcifications is clearly visible in the details band.

For wavelets close in form to the Laplacian of Gaussian, the details filters can be expressed as point spread functions

$$p^j_{\text{LH}}(x,y) = -\frac{\partial^2}{\partial y^2}\gamma(x,y)$$

$$p^j_{\text{HL}}(x,y) = -\frac{\partial^2}{\partial x^2}\gamma(x,y)$$

$$p^j_{\text{HH}}(x,y) = \frac{\partial^4}{\partial x^2 \partial y^2}\gamma(x,y) \qquad (10)$$

where $\gamma(x,y) = e^{-((x^2+y^2)/2\sigma^2)}$ and $\sigma$ depends on octave $j$. The transfer functions corresponding to the components $d^j_{\text{HH}}$ and $d^j_{\text{LH}} + d^j_{\text{HL}}$ compute to be

$$P^j_{\text{HH}}(\omega_x, \omega_y) = \omega_x^2 \omega_y^2 e^{-(\sigma^2(\omega_x^2 + \omega_y^2)/2)}$$

$$P^j_{\text{LH}}(\omega_x, \omega_y) + P^j_{\text{HL}}(\omega_x, \omega_y) = (\omega_x^2 + \omega_y^2)e^{-(\sigma^2(\omega_x^2 + \omega_y^2)/2)}.$$

$$(11)$$

For $\alpha \ll 1$—a realistic assumption—these details filters have the same form as the separable and nonseparable matched

filters in (2) and (5), respectively. The biorthogonal spline wavelet basis of [36] and [40] is close in form to the Laplacian of Gaussian and therefore appropriate for multiscale matched filtering. Fig. 6 compares the separable HH details filter $p^j_{\text{HH}}(x, 0)$ resulting from the biorthogonal spline wavelet with the separable matched filter $h_{mf}(x)$ in (2). The details filter is a close approximation to the matched filter over four octaves. (Only the separable filters are shown since they can be represented in one dimension and thus easily compared. Similar comments apply to the nonseparable LH+HL details filter and the nonseparable matched filter.) The closest match between (11), (2), and (5) occurs when the Markov noise is highly correlated with $\alpha \ll 1$. We have seen this to be true of the Nijmegen database. In this noise regime a multiscale image decomposition with the above biorthogonal spline wavelet creates a sequence of HH and LH+HL details subimages which is equivalent to applying the matched filters in (2) and (5) at increasing scale. The smallest $\mu$Ca++s appear in the high-frequency octaves and vice versa.
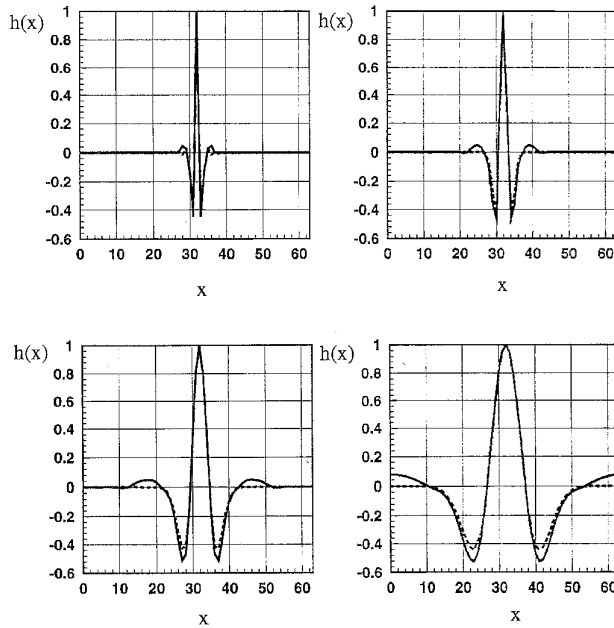
Fig. 6. Comparison of the point spread functions of the separable details filter $p^j_{HH}(x, 0)$ (solid) and the separable matched filter $h_{mf}(x)$ (broken) across four octaves, shown from upper left to lower right.

Microcalcifications of a certain size give rise to a strong peak response in both HH and LH+HL at the corresponding octave level. Computing a combination of both responses provides an even stronger indication of the presence and location of $\mu$Ca++s. As shown in Fig. 2, the combination of separable and nonseparable filter responses is supported by the composite texture model of breast tissue.

To justify this combination of matched filter forms, we compare the detection performance of the wavelet method with that of the matched filters by computing ROC curves (Fig. 7) using simulated Gaussian objects embedded in both separable and nonseparable Markov noise. The SNR used is 0.2 (peak object intensity $\div \sigma_n$) and the Markov correlation parameter $\alpha = 0.01$. Since the objects are of fixed size in the test only one octave band of the wavelet decomposition is involved in the ROC computation. The performance of the $P^j_{HH}(\omega_x, \omega_y)$ filter is almost identical to that of the matched filter based on separable noise. Likewise, the LH+HL results compare to those of the matched filter based on nonseparable noise.

### D. Threshold Model

The responses of the individual wavelet matched filters must be pooled to produce a detection decision. The simplest approach is a *threshold model*, which has its roots in spatial frequency channel models of the human visual system [41]. The output of each matched filter, corresponding to a specific frequency band, is first thresholded to produce a one (detect) or zero (no detect) result. The binary outputs from all channels are then combined by the rule of probability summation: the probability of detection for the system is the sum of the probabilities of detection for each channel. The final test
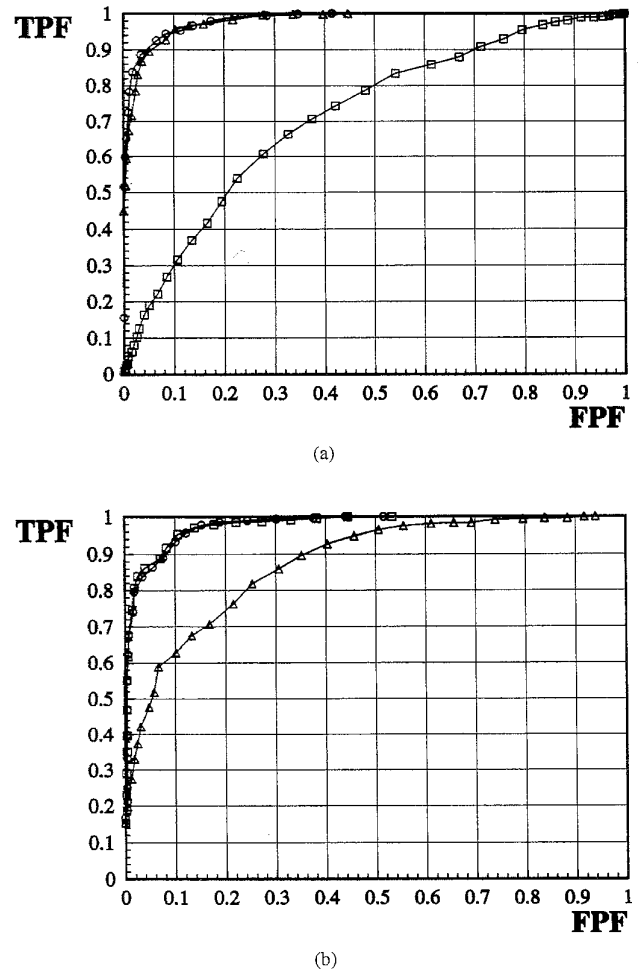


(a)



(b)

Fig. 7. Justifying the use of both separable and nonseparable matched filters. ROC performance of matched filter ($\circ$), HH details filter ($\triangle$), and LH+HL details filter ($\square$). Tests were performed on the detection of Gaussian objects in simulated (a) separable, (b) nonseparable Markov noise. In (a) the HH filter and in (b) the LH+HL filters are close to optimum.

statistic, which is the sum of the binary outputs, is then thresholded to give the final detection decision. In our work we employ eight spatial frequency bands, corresponding to four octaves with two matched filter outputs $\left( d^j_{HH}, d^j_{LH+HL} \right)$ per octave. Hence, the pooled test statistic at each pixel location is a number between zero and eight. We make a detect decision when this number is three or above.

Selecting a uniform threshold for the individual matched filter outputs is made difficult by variations in dynamic range and histogram shape from one sub-band to the next. Our solution is to use a threshold corresponding to a fixed percentile of the histogram of each matched filter output. A potential drawback of this approach is that a certain number of pixels are always detected at each threshold. The probability summation, however, acts as a check: only those pixels being detected in three or more channels are admitted to the final map of $\mu$Ca++s. The percentile threshold is varied during computation of the detector performance curve. The selection of a working threshold for the algorithm depends on the desired specificity of the overall system.

## E. Summary of Detection Algorithm

To recap, we employ a four octave sub-band decomposition, implemented at full resolution with an intermediate voice computed between octaves 2 and 3 and one between octaves 3 and 4. As a result of using the biorthogonal spline wavelet [36], the separable 2-D filters in (8) which transform the input image into the HH, LH, HL (and hence LH+HL) details sub-bands are closely related to prewhitening matched filters for detecting Gaussian objects in two kinds of first order Markov noise. A blend of the two noise types is a reasonable model for high frequency breast texture. This analysis phase of the computation is equivalent to a bank of multiscale matched filters for detecting objects of diameter 100 $\mu$m $\rightarrow$ 1 $\mu$m.

The algorithm proceeds as follows. (See Fig. 8.) The outputs $d^j_{HH}, d^j_{LH+HL}$ from all four octaves are thresholded at some fixed percentile of the histogram of each component. The detected (binary) images from all octaves are then summed to give, at each pixel, a number between zero and eight. Pixels with value three or greater are admitted to the final detection map. If segmentation of $\mu$Ca++s is desired, and since matched filter detectors do not preserve $\mu$Ca++ shape, a second step is required. First, a circular region centered at each detected pixel site is weighted (typically by 20); then a straightforward inverse wavelet transform of the LL image from octave 4 and the detection-enhanced details subimages from octaves 1 through 4 (plus two voices) reconstructs the original mammogram with detected $\mu$Ca++s visible. This form of output may be useful where further viewing by the radiologist is required, since the context of the detected pixels within the breast will probably be required for diagnosis purposes. Alternatively, the smooth (LL) subimage may be omitted in computing the inverse transform, leaving an image containing only suspected $\mu$Ca++s. The diameter of the circular weighting region increases with octave, and hence object scale.

## V. RESULTS

We have tested our method on the Nijmegen database of 40 mammograms [19]. Regions of film outside the breast tissue were identified by hand and not processed. The free-response receiver operating characteristic (FROC) [42] curves in Fig. 9 were generated by counting true positive (TP) and false positive (FP) clusters for each mammogram while varying the percentile threshold applied to the sub-band images. The percentile ranged from 0.9980 to 0.9999. (Fig. 8 indicates the stage in processing at which FROC is computed. The working threshold of the system depends on the acceptable false positive rate.)

To demonstrate the impact of the images numbered 12o and 12c, Fig. 9 also shows an FROC curve computed when these images were omitted from the test. As stated earlier, this image pair accounts for 27% of the total clusters in the database. Furthermore, many of these clusters are closely grouped or partly overlapping, and many $\mu$Ca++s fall outside the truth circles marked by the radiologists. These $\mu$Ca++s are often



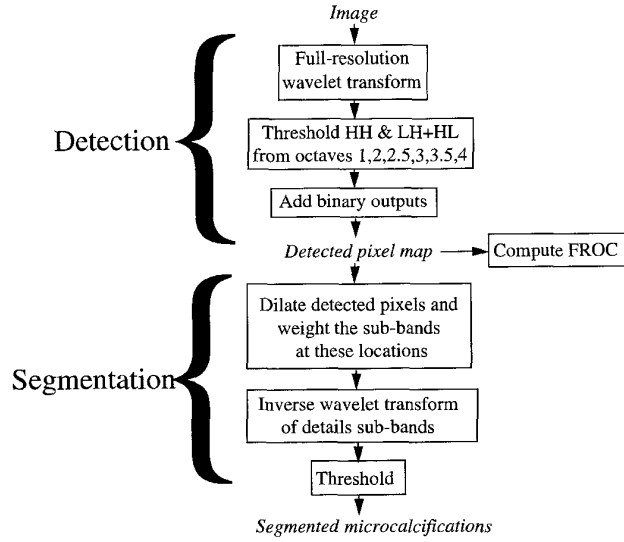Fig. 8. Summary of algorithm for detecting and segmenting microcalcifications.



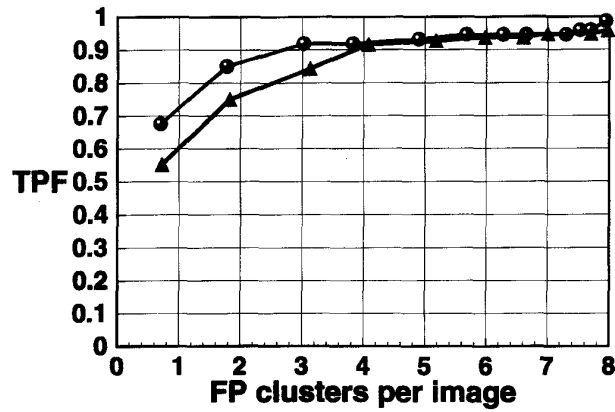Fig. 9. Cluster detection performance measured on 40 mammograms. ($\triangle$)—All 40 images were used. (o)—Images 12o, 12c were omitted from testing. Clearly, these images have a major impact on both the database and the results.

detected, resulting in a higher false positive rate, and an overall drop in FROC performance.

Examples showing $\mu$Ca++s reconstructed by the second, segmentation step are given in Fig. 10. Notice that, although the matched filter is predicated on circular $\mu$Ca++s, the segmentation process is able to reconstruct $\mu$Ca++s of arbitrary shape. This can be explained as follows. The matched filter, although designed for detecting objects of Gaussian shape, nevertheless produces a significant peak response to objects of similar shape and of the same size as the Gaussian. However, the shape of the matched filter response is not an estimate of the object; it is the location and height of the peak value that is significant. Hence, when thresholded, the matched filter output is typically smaller than the object to be detected. By dilating each detected pixel, we effectively "cast a net" encircling that location to find the object responsible for the output peak at that point. This process of weighting circular regions centered on detected pixels is analogous to filtering in
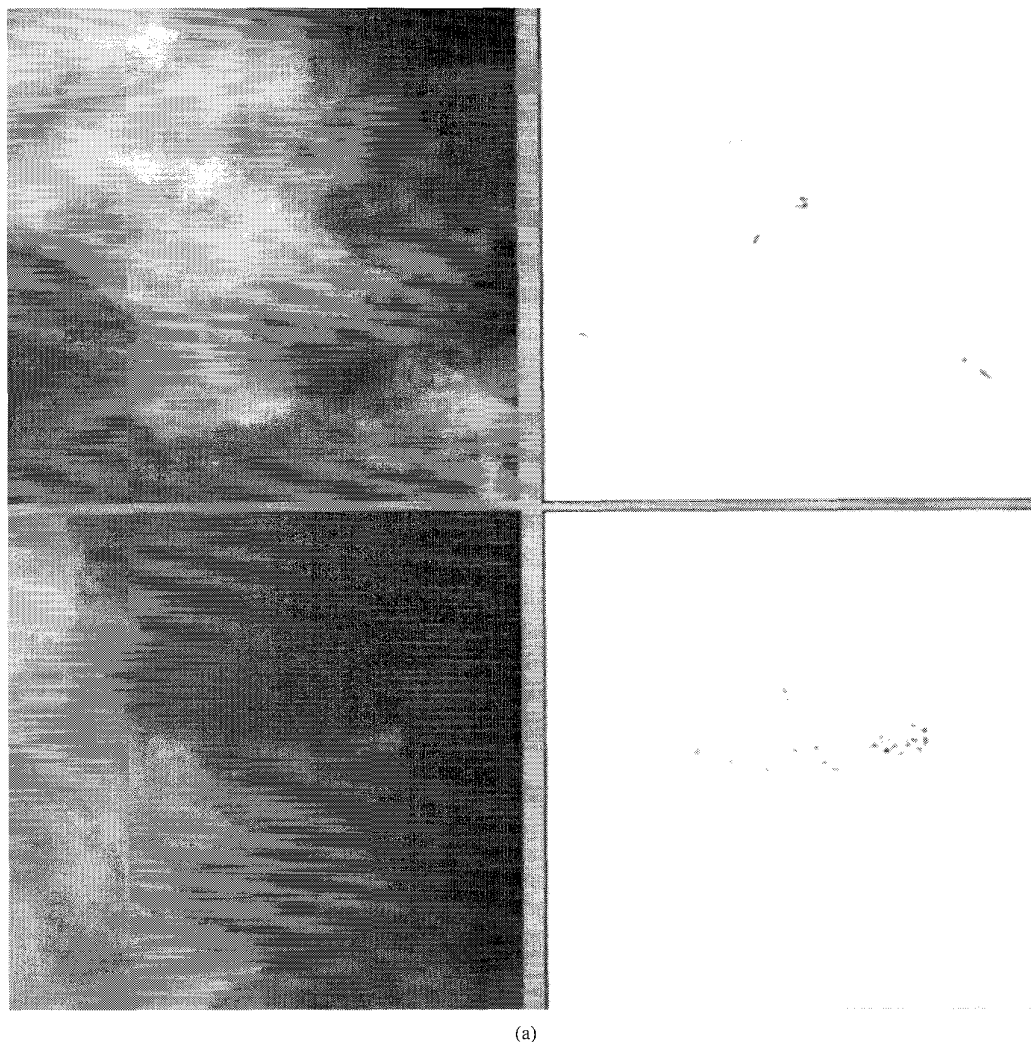
(a)

Fig. 10. Examples of microcalcification clusters reconstructed using the complete algorithm shown in Fig. 8. In each case an original 512 × 512 pixel mammogram section and the recovered microcalcifications are shown. (a) One example shows scattered microcalcifications, the other a well defined cluster. (b), (c) Magnified sections of the examples in (a), clearly showing that calcification shape is recoverable. (The original mammograms are shown contrast-enhanced for display purposes.)

the Fourier domain, except that the wavelet transform occupies a domain whose coordinates are space and scale. The fact that elongated calcifications can be recovered by our approach can be explained by noting that fine, linear structures may in some cases be modeled by superposing Gaussian functions of appropriate scale along a line or curve.

To justify the inverse wavelet transform stage, we present another close-up example of segmented $\mu$Ca++s in Fig. 11. The calcification boundaries generated by the second, segmentation step are visibly more accurate than those present in the detected pixel map created by the first stage.

## VI. DISCUSSION AND CONCLUSIONS

With an appropriate choice of wavelet basis the undecimated wavelet transform with inter-octave voicing can be a useful tool for detecting $\mu$Ca++s in digitized mammograms. The method uses multiscale matched filters designed for detecting Gaussian objects in correlated Markov noise. The classical

matched filter used in communications receivers makes no attempt to recover the shape of the incoming signal. Likewise, while the first (analysis) stage of our method *detects* the presence of $\mu$Ca++s, it does not accurately segment them. However, by weighting the details sub-bands at the sites of detected pixels followed by computing the inverse wavelet transform we achieve a reasonable segmentation of $\mu$Ca++ outlines. The detection performance of the method has been tested by computing FROC curves using the Nijmegen database of 40 mammograms. Several qualitative examples of segmented clusters are presented as evidence that $\mu$Ca++s of varied shape can be recovered.

The method requires computing one four-octave wavelet transform, one three-octave wavelet transform (for the inter-octave voices), and one inverse wavelet transform if accurate $\mu$Ca++ segmentation (as opposed to just detection) is desired. Efficient wavelet transform techniques are employed through-
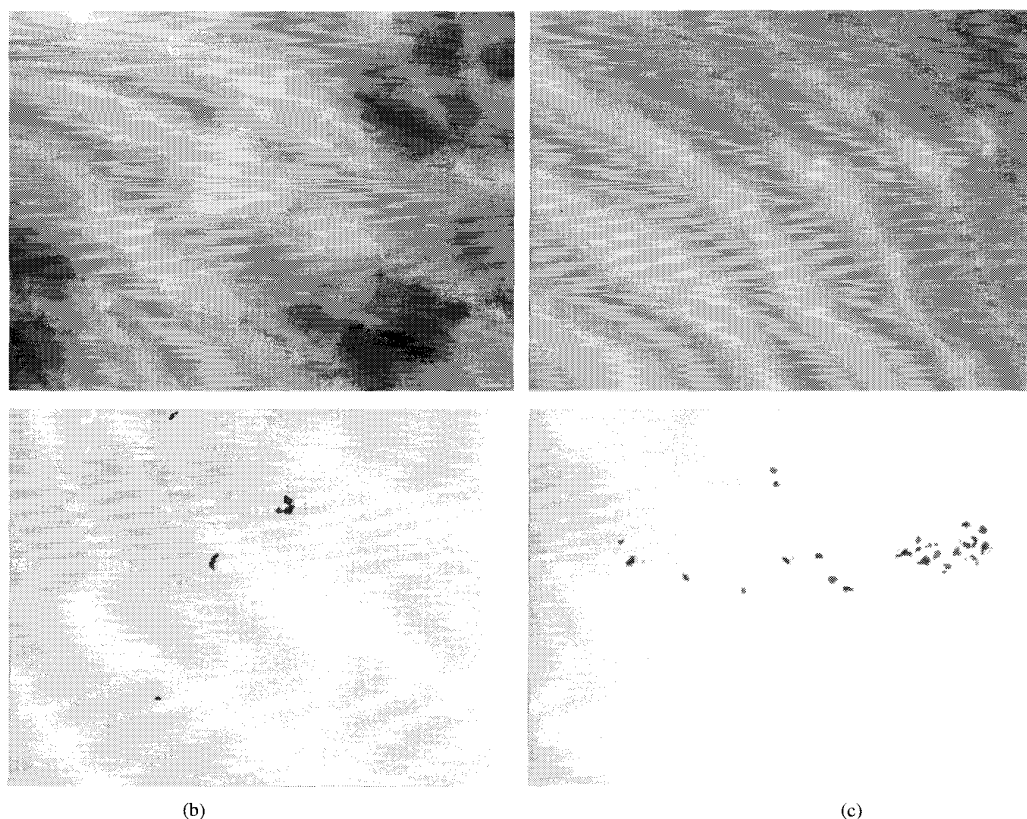
(b)        (c)

Fig. 10. *(Continued).*

out. In practice we notice little drop in detection results when we omit the contributions from HH and LH+HL in octaves 1 and 4. Hence octave 4 need not be computed, whereas octave 1 is required in the sub-band decomposition. Octaves 2, 2.5, 3, and 3.5 are required to obtain best performance at the working resolution of the Nijmegen database. Further work is needed to ascertain the optimum sampling of this scale range.

The weighting factor applied during the reconstruction stage influences the contrast of the segmented $\mu$Ca++s relative to the background. We currently use a factor of 20. The smaller the value used, the more noticeable the background breast texture appears, and vice versa. As stated earlier, we usually omit the LL component in the final reconstruction, unless the context of the large scale breast structure is deemed to be valuable in a given situation, such as for viewing by a radiologist.

When tested on the same database, Karssemeijer's detection method, which integrates Bayesian techniques with random field models [19], [20], detects approximately 82% of true clusters at a false positive rate of 0.7 clusters per image. This is significantly better than our detection rate of 55% true positives at the same false positive rate, computed using the entire database of 40 images.[1] Karssemeijer's approach gains this advantage by: 1) using a neighborhood interaction mechanism which disallows

[1] In earlier work [43] we reported a higher detection rate for the same database. Later, we found our cluster counting code to be unreliable. We now use code supplied by Karssemeijer.

detected pixels from regions containing both calcifications and linear structure, and 2) rewarding detected pixels which occur in local clusters. Action 1) reduces the number of false positives due to long strands of connective tissue, and action 2) tends to eliminate many isolated false detections.

The proposed method is founded on the principles of optimum detectors (matched filters); furthermore, the analysis/synthesis paradigm of the wavelet transform is elegant, simple to implement, and affords the potential for future enhancements of the basic approach. For example, the wavelet basis used here, being close to the Laplacian of Gaussian, provides useful zero-crossing information in the details LH+HL sub-bands which could be applied to the suppression of false edges and lines. The sub-bands could also be scanned for, and weighting applied to, clusters of detected pixels, prior to the inverse wavelet transform step. (The current method applies equal weight to *all* detected pixels, whether isolated or clustered.) As well, future work will address the potential of using multiple wavelet bases for computing multiple forward wavelet transforms. The idea here is that different wavelets may target different object classes. For example, a given wavelet may be more appropriate for enhancing the background texture in mammograms. By combining sub-bands from the multiple transforms it is conceivable that background structures could be favorably suppressed. Significantly, only one set of sub-bands needs to be involved in the reconstruction (inverse wavelet transform) stage.

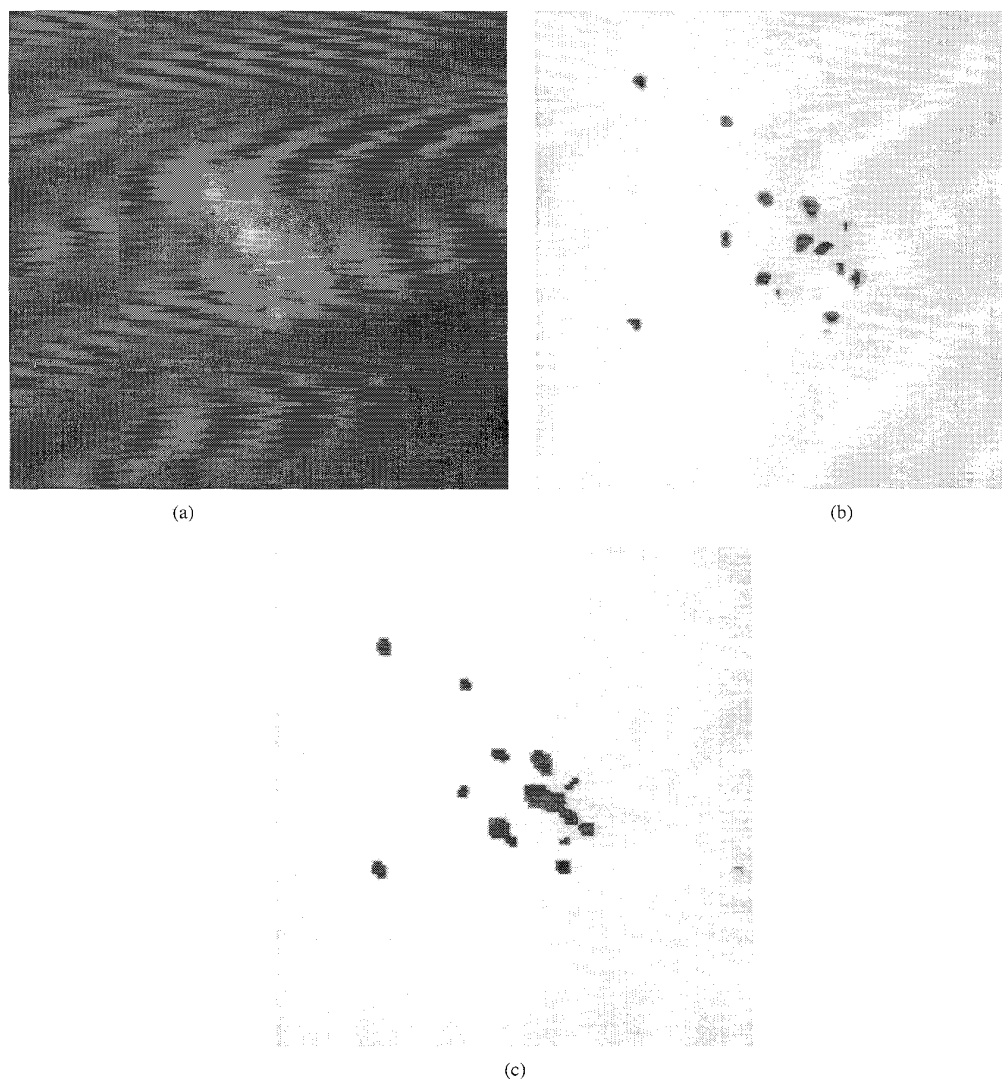(a)                                                            (b)

(c)

Fig. 11. (a) The original mammogram section. (b) Close-up view of a cluster showing that microcalcifications are more accurately segmented when the secon stage processing is implemented (weight/inverse wavelet transform/threshold), compared to (c) the detected pixel map generated by the first stage. (See Fig. 8.

## REFERENCES

[1] L. W. Bassett, "Mammographic analysis of calcifications," *Radiol. Clin. No. Amer.*, vol. 30, pp. 93–105, 1992.
[2] S. Eideken, "Mammography and palpable cancer of the breast," *Cancer*, vol. 61, pp. 263–265, 1988.
[3] R. I. Egan, M. B. McSweeney, and C.W. Sewell , "Intramammary calcifications without an associated mass in benign and malignant diseases," *Radiol.*, vol. 137, pp. 1–7, 1980.
[4] M.Lanyi, *Diagnosis and Differential Diagnosis of Breast Calcifications.* Springer-Verlag, Berlin, 1986.
[5] M. J. Lopez and C. W. Blackwell, "Breast cancer detected by screening: The importance of long-term follow-up," *Surg.*, vol. 106, pp. 590–595, 1989.
[6] E. A. Sickles,"Breast calcifications: Mammographic evaluation," *Radiol.*, vol. 160, pp. 289–293, 1986.

[7] C. J. Baines, A. B. Miller, C. Wall, D. V. McFarlane, I. S. Simo R. Jong, B. J. Shapiro, L. Audet, M. Petitclerc, D. Ouimet-Oliv J. Ladouceur, G. Hebert, T. Minuk, G. Hardy, and H. K. Standin "Sensitivity and specificity of first screen mammography in the Canadia national breast screening study," *Radiol.*, vol. 160, pp. 295–298, 198
[8] C. J. Baines, D. V. McFarlane, and A. B. Miller, "The role of th reference radiologist: Estimates of interobserver agreement and potenti delay in cancer detection in the national screening study," *Investiga Radiol.*, vol. 25, pp. 971–976, 1990.
[9] L. W. Bassett, D. H. Bunnell, R. Jahanshahi, R. H. Gold, R. D. Arnd and J. Linsman, "Breast cancer detection: One versus two views, *Radiol.*, vol. 165, pp. 95–97, 1987.
[10] P. H. Peeters, A. L. Verbeek, J. H. Hendriks, R. Holland, M. Mravuna( and G. P. Vooijis, "The occurrence of interval cancers in the Nijmege screening programme," *British J. Cancer*, vol. 69, pp. 929–932, 1989.
[11] E. Silverberg, C. C. Boring, and T. S. Squires, "Cancer statistics, 1990, *Ca-A J. Clinicians*, vol. 40, pp. 9–26, 1990.
[12] H. P. Chan, K. Doi, S. Galhotra, C. J. Vyborny, H. MacMahon, an P.M. Jokich, "Image feature analysis and computer-aided diagnosis i digital radiography: 1. Automated detection of microcalcifications i mammography," *Med. Phys.*, vol. 14, pp. 538–548, 1987.
[13] H. P. Chan, K. Doi, C. J. Vyborny, K. L. Lam, and R. A. Schmid "Computer-aided detection of microcalcifications in mammogram: Methodology and preliminary clinical study," *Investigat. Radiol.*, vo 23, pp. 664–671, 1988.

[14] H. P. Chan, K. Doi, C. J. Vyborny, R. A. Schmidt, C. E. Metz, K. L. Lam, T. Ogura, Y. Wu. and H. MacMahon, "Improvement in radiologists' detection of clustered microcalcifications on mammograms: The potential of computer-aided diagnosis," *Investigat. Radiol.*, vol. 25, pp. 1102–1110, 1990.

[15] R. M. Nishikawa, M. L. Giger, K. Doi, C. J. Vyborny, R. A. Schmidt, C. E. Metz, Y. Wu, F.-F. Yin, Y. Jiang, Z. Huo, P. Lu, W. Zhang, T. Ema, U. Bick, J. Papaioannou, and R. H. Nagel, "Computer-aided detection and diagnosis of masses and clustered microcalcifications from digital mammograms," in *Biomedical Image Processing and Biomedical Visualization, Proc. SPIE 1905*, R. S. Acharya and D. B. Goldgof, Eds. , 1993, pp. 442–432.

[16] K. S. Woods, J. L. Solka, C. E. Priebe, W. P. Kegelmeyer, C. C. Doss and K. W. Bowyer, "Comparative Evaluation of Pattern Recognition Techniques for Detection of Microcalcifications in Mammography," *Int. J. Pattern Recognition Artificial Intell.*, vol. 7, Dec. 1993.

[17] W. P. Kegelmeyer and M. C. Allmen, "Dense feature maps for detection of microcalcifications," in *Proceedings Second International Workshop on Digital Mammography*. Amsterdam, the Netherlands: Elsevier, 1994, pp. 3–12.

[18] B. W. Fam, S. L. Olson, P. F. Winter, and F. J. Scholz, "Algorithm for the detection of fine clustered calcifications in film mammograms," *Radiol.*, vol. 169, pp. 333–337, 1988.

[19] N. Karssemeijer, "A stochastic model for automated detection of calcifications in digital mammograms," in *Proc. 12th Int. Conf. Inform. Processing Med. Imag.*, Wye, UK, pp. 227–238, 1991.

[20] N. Karssemeijer, "Adaptive noise equalization and image analysis in mammography," in *13th Int. Conf. Inform. Processing Med. Imag.*, Flagstaff, AZ, 1992, pp. 472–486. (The Nijmegen database is available by anonymous FTP from *figment.csee.usf.edu*.)

[21] A. G. Gale, E. J. Roebuck, P. Riley, and B. S. Worthington, "Computer aids to mammographic diagnosis," *British J. Radiol.*, vol. 60, pp. 887–891, 1987.

[22] B. Reeves, A. G. Gale, E. J. Roebuck and A. R. M. Wilson, "Breast screening: Deciphering the structure of mammographic microcalcification," *British J. Radiol.*, vol. 65, p. 96, 1992.

[23] D. H. Davies, and D. R. Dance, "Automatic computer detection of clustered calcifications in digital mammograms," *Phys. Med. Biol.*, vol. 35, pp. 1111–1118, 1990.

[24] W. Richardson, "Nonlinear filtering and multiscale texture discrimination for mammograms," in *Mathematical Methods Med. Imag*, D. C. Wilson and J. N. Wilson, Eds. *Proc. SPIE 1768*, 1992, pp. 293–305.

[25] A. Laine and S. Song, "Multiscale wavelet representations for mammographic feature analysis," in *Mathematical Methods Med. Imag.*, D. C. Wilson and J. N. Wilson, Eds. *Proc. SPIE 1768*, 1992, pp. 306–316.

[26] A. Laine, J. Fan, and S. Schuler, "A framework for contrast enhancement by dyadic wavelet analysis," *Proc. 2nd Int. Workshop on Digital Mammography*, A. G. Gale *et al.*, Eds., pp. 91–100.

[27] H. Barman, and G. Granlund, "Using simple local Fourier domain models for computer-aided analysis of mammograms," in *Proc. 8th Scandinavian Conf. Image Anal.*, Tromso, Norway, May, 1993, pp. 479–486.

[28] W. Qian, P. Clarke, M. Kallergi, H.-D. Li, R. Velthuizen, R. A. Clark, and M. L. Silbiger, "Tree-structured nonlinear filter and wavelet transform for microcalcification segmentation in mammography," in *Biomedical Image Processing and Biomedical Visualization*, R. S. Acharya and D. B. Goldgof, Eds. Proc. SPIE 1905, 1993, pp. 509–520.

[29] Y. Yoshida, K. Doi, R. M. Nishikawa, T. Ema and W. Zhang, "Automated detection of clustered microcalcifications in digital mammograms using wavelet processing techniques," in *Medical Imaging*, Proc. SPIE 2167, 1994, pp. 868–886.

[30] W. K. Pratt, *Digital Image Processing*, 2nd ed. New York: Wiley, 1991.

[31] R. N. Strickland, "Detecting tumors in nonstationary backgrounds," *IEEE Trans. Med. Imag.*, vol. 13, no. 3, pp. 491–499, Sept. 1994.

[32] B. R. Hunt and T. M. Cannon, "Nonstationary assumptions for Gaussian models of images," *IEEE Trans. Syst., Man, and Cybern.*, vol. SMC-6, pp. 876–882, Dec. 1976.

[33] A. K. Jain, *Fundamentals of Digital Image Processing*. Englewood Cliffs, NJ: Prentice-Hall, p. 403, 1989.

[34] R. N. Strickland, "Transforming images into block stationary behavior," *Appl. Opt.*, vol. 22, no. 10, pp. 1462–1473, May 1983.

[35] R. A. Gopinath and C. S. Burrus, "A tutorial overview of filter banks, wavelets and interrelations," Dept. of Elec. and Comp. Eng., Rice Univ., Houston, TX 77251, Tech. Rep. TR93-01, 1993.

[36] A. Cohen, I. Daubechies, and J. C. Feauveau, "Biorthogonal bases of compactly supported wavelets," AT&T Bell Lab., Tech. Rep., TM 11217-900529-07, 1990.

[37] M. J. Shensa, "The discrete wavelet transform: Wedding the à trous and Mallat algorithms," *IEEE Trans. Signal Processing*, vol. 40, pp. 2464–2482, Oct. 1992.

[38] O. Rioul and P. Duhamel, "Fast algorithms for discrete and continuous wavelet transforms," *IEEE Trans. Inform. Theory*, vol. 38, no. 2, pp. 569–586, Mar. 1992.

[39] S. Mallat,"Zero-crossings of a wavelet transform," *IEEE Trans. Inform. Theory*, vol. 37, no. 4, pp. 1019–1033, July 1991.

[40] M. Antonini, M. Barlaud, P. Mathieu and I. Daubechies, "Image coding using wavelet transform," *IEEE Trans. Image Processing*, vol. 1, no. 2, pp. 205–220, Apr. 1992.

[41] R. F. Quick, "A vector magnitude model of contrast detection," *Kybernetic*, vol. 16, pp. 65–67, 1974.

[42] P. C. Bunch, J. F. Hamilton, G. K. Sanderson and A. H. Simmons, "A free-response approach to the measurement and characterization of radiographic-observer performance," *J. Appl. Photogr. Eng.*, vol. 4, pp. 166–171, 1978.

[43] R. N. Strickland and H. I. Hahn, "Detection of microcalcifications using wavelets," in *Proc. 2nd Int. Workshop Dig. Mammogr.*, July 1994.